Available online at www.sciencedirect.com

ScienceDirect

Ceramics International 40 (2014) 2349–2358

CERAMICS INTERNATIONAL

www.elsevier.com/locate/ceramint

Preparation, characterization and electrical conductivity studies of nanocrystalline scheelite $Ba_{1-x}Dy_xMoO_{4+\delta}$

Paramananda Jena[a], N. Nallamuthu[a], M. Venketswarulu[b], N. Satyanarayana[a,*]

[a]Department of Physics, Pondicherry University, Pondicherry 605014, India
[b]R&D Amara Raja Batteries Ltd., Tirupati 517501, AP, India

Received 16 July 2013; received in revised form 18 July 2013; accepted 1 August 2013
Available online 22 August 2013

Abstract

Nanocrystalline Dy doped $BaMoO_4$ [$Ba_{1-x}Dy_xMoO_{4+x/2}$, where $x=0$, 0.05, 0.1, 0.15, and 0.2] samples were prepared by the acrylamide assisted sol–gel process. The prepared samples were characterized by TG/DTA, XRD, FTIR, SEM-EDX and XRF techniques. From XRD patterns, crystalline phases for $Ba_{1-x}Dy_xMoO_{4+x/2}$, where $x=0$, 0.05, 0.1, 0.15, and 0.2 were confirmed and their average crystallite sizes calculated using Scherrer's formula were found to be less than 80 nm. Thermal behavior and structure of Scheelite type nanocrystalline $Ba_{1-x}Dy_xMoO_{4+x/2}$, where $x=0$, 0.05, 0.1, 0.15, and 0.2 samples were identified using TG/DTA and FTIR measurements respectively. Microstructure and existence of O, Dy, Ba, and Mo in the Dy doped $BaMoO_4$ samples were obtained from SEM-EDX and XRF results. The electrical conductivities of different compositions of the prepared nanocrystslline Dy doped $BaMoO_4$ samples were evaluated by analyzing impedance data as a function temperature ranging from 350 to 650 °C under air using winfit software. Among the doped compositions, $Ba_{0.90}Dy_{0.10}MoO_{4+\delta}$ exhibited high conductivity of 5.46×10^{-3} S/cm at 650 °C.

Keywords: A. Sol–gel processes; C. Electrical conductivity; C. Impedance; E. Fuel cells

1. Introduction

Oxygen ion conducting solid electrolytes have many device applications such as sensors, solid oxide fuel cells, oxygen pumps, electrochemical reactors, steam electrolysis cells, etc. [1,2]. Several families of oxygen ion conducting materials have been investigated for intermediated temperature solid oxide fuel cells (ITSOFs) like fluorite type (stabilized ZrO_2, CeO_2 and δ-Bi_2O_3), pervoksite type ($LaGaO_3$, $BaCeO_3$ and $SrCeO_3$), brownimillerite type ($Ba_2Ln_2O_3$), Aurivillus type (BIMEVOX), Pyrochlore type ($Gd_2Zr_2O_7$) and Scheelite type oxides [3–5]. Among these, Scheelite type oxide materials exhibit high ion conductivity, which are comparable with the conventional oxide ion conductors like yttria stabilized zirconia. Scheelite-type materials are tetragonal structure characterized by the general formula ABO_4 (A=Ca, Sr, Ba; B=Mo, W), space group $I4_1/a$ and Symmetry C^{4h} [6]. Some of the doped ABO_4 (A=Ca, Sr, Ba; B=Mo, W) Scheelite type materials have been investigated and studied their high oxide ion conduction at intermediate temperature range [7–15].

In recent years, nanostructure ceramics have been investigated due to the presence of the large fraction of grain boundaries that can lead to remarkable enhanced electrical, mechanical, magnetic, optical sensing and biomedical properties compared with the microstructure samples [16]. Nanocrystalline Scheelite type metal oxide can be prepared using different techniques. Preparation using the conventional solid state reaction method involves high temperature heating of oxide or carbonate precursors, which exhibit more disadvantages like inhomogeneity, abnormal grain growth, poor stoichiometry, etc. [17]. These difficulties could be avoided using wet chemical methods such as sol–gel combustion, co-precipitation, hydrothermal reaction, etc. [18–20]. Sol–gel combustion is a very simple, cost effective and versatile process for the preparation of multicomponent nanocrystalline metal oxides, in which citric acid used as fuel as well as chelating agent [21–23]. However, the nanocrystalline metal oxides prepared using citric acid assisted gel combustion process

*Corresponding author. Tel.: +91 413 2654404; fax: +91 413 2655348.
E-mail addresses: parama.pondy@gmail.com (P. Jena), nallanis2011@gmail.com (N. Satyanarayana).

0272-8842/$ - see front matter © 2013 Elsevier Ltd and Techna Group S.r.l. All rights reserved.
http://dx.doi.org/10.1016/j.ceramint.2013.08.005

has some drawbacks such as presence of impurity phase as well as residual organics due to the prolonged multi step combustion mechanism [24]. The acrylamide (dual fuel) assisted gel combustion process, in which acrylamide acts as fuel along with citric acid, yields phase pure organic free nanocrystalline metal oxides at lower temperature.

In the present study, different compositions of nanocrystalline Dy doped $BaMoO_4$ [$Ba_{1-x}Dy_xMoO_{4+x/2}$, where $x=0$ (BMO), 0.05 (BDM0.05), 0.1 (BDM0.1), 0.15 (BDM0.15), and 0.2 (BDM0.2)] samples are prepared using the acrylamide assisted sol–gel combustion process and are characterized by using TG/DTA, XRD, FTIR, SEM-EDX and XRF techniques. Impedance data were measured as a function of temperature ranging from 350 to 650 °C for the sintered Dy doped $BaMoO_4$ pellets under air and the electrical conductivity was evaluated by analyzing the measured impedance data using winfit software.

2. Experimental method

2.1. Sol–gel combustion process

Different compositions of nanocrystalline Dy doped $BaMoO_4$ [$Ba_{1-x}Dy_xMoO_{4+x/2}$, where $x=0$ (BMO), 0.05 (BDM0.05), 0.1 (BDM0.1), 0.15 (BDM0.15), and 0.2 (BDM0.2)] samples were synthesized using the acrylamide assisted sol–gel combustion process. Analar grade precursor chemicals such as barium nitrate (Qualigens, India), dysprosium nitrate (Sigma Aldrich, Australia), ammonium molybdate (Loba Chemie, India), with Acrylamide [Ac] (Qualigens, India) and citric acid [CA] (Qualigens, India) as fuels were used in the sol–gel process. The precursor chemicals (barium nitrate, dysprosium nitrate and ammonium molybdate) are taken according to their respective molecular weight percentages and the fuels (acrylamide and citric acid) are also varied according to the molar ratio of metal ions [M] to fuel ratio (M:Ac:CA = 1:1:1). Required quantity of barium nitrate is dissolved in distilled water and mixed with citric acid and acrylamide solutions. Dysprosium nitrate solution is prepared by dissolving the required amount of dysprosium nitrate in the distilled water. Ammonium molybdate is dissolved in distilled water and formed the transparent solution. Half an hour later, dysprosium nitrate and barium nitrate solutions were added to the ammonium molybdate solution and stirred continuously at 80 °C, till the formation of gel. The prepared gels are calcined and characterized using TG/DTA, XRD, FTIR, SEM-EDX and XRF techniques.

2.2. Measurement techniques

Thermogravimetric/differential thermal analysis (TG/DTA) curves of the calcined gel samples are recorded at the heating rate of 10 °C/min between 30 °C and 900 °C in nitrogen atmosphere using TA instrument model no SDT Q600 V20.5. Powder X-ray diffraction (XRD) patterns are recorded using X'Pert PRO MPD, PANalytical X-ray powder diffractometer employing Cu Kα radiation ($\lambda=0.15406$ nm), angles ranging from 10° to 80° with step size 0.02. The average crystallite sizes of different compositions of Dy doped $BaMoO_4$ samples are calculated using Scherrer's formula. Fourier Transform Infrared (FTIR) Spectra are recorded using a Thermo Nicolet FTIR-6700 spectrometer from 4000 cm^{-1} to 400 cm^{-1} for 32 scans. Microstructure and existence of elements O, Dy, Ba and Mo in the Dy doped $BaMoO_4$ samples are obtained using SEM-EDX [Hitachi-450 model]. The samples are spread on the conducting carbon tape pasted over the aluminum stub and a thin layer of gold was coated over the sample using plasma sputtering for taking SEM-EDX. The presence of Dy_2O_3, BaO and MoO_3 for the various compositions of Dy doped $BaMoO_4$ samples are obtained using an X-ray Fluorescence spectrometre (Bruker S4-Pioneer model). For conductivity measurement, the prepared Dy doped nanocrystalline $BaMoO_4$ powders were pressed into 10 mm diameter and 1–3 mm thickness pellet at 4000 kg/cm^2 using KBr Hydraulic press. The pellets were heated to 900 °C in air at heating rate of 10 °C/min and sintered for 12 h then cooling down to room temperature naturally (furnace: Rands Instruments Company, Chennai, India, DTC324). Silver paste is painted on both side of sintered $BaMoO_4$ and Dy doped $BaMoO_4$ pellets sample as electrodes and heated at 200 °C for half an hour to ensure maximum contact and adherence. Impedance [real (Z') and imaginary (Z'')] data are measured for all the pellets using a Novocontrol Alpha A High performance frequency analyzer in the frequency range 10 MHz–0.2 Hz at different temperatures. The measured impedance data are analyzed using winfit software to obtain the resistance for calculating the conductivity and activation energy of the nanocrystalline $BaMoO_4$ and Dy doped $BaMoO_4$ samples.

3. Results and discussion

3.1. TG/DTA

Thermogravimetric/Differential thermal analysis curves (TG/DTA) for the different compositions of Dy doped $BaMoO_4$ [$Ba_{1-x}Dy_xMoO_{4+x/2}$, where $x=0$ (BMO), 0.05 (BDM0.05), 0.1 (BDM0.1), 0.15 (BDM0.15), and 0.2 (BDM0.2)] dried gel samples are shown in Fig. 1. The observed two broad endothermic peaks between 40 °C and 145 °C and the corresponding weight losses are due to the evaporation of water molecules existing in the dried gel samples. From Fig. 1, in all TG/DTA curves, the observed exothermic peak at 178 °C is due to the decomposition of citric acid and decomposition of the nitrates from the barium nitrate as well as from dysprosium nitrate and its intensified with the increase of the dysprosium content in the $BaMoO_4$ sample. Doping of dysprosium in $BaMoO_4$ increases the total quantity of nitrates in the precursor, which increases the oxidant ratio and helpful for combustion reaction. In all TG/DTA curves, the observed exothermic curve at ~570 °C and the corresponding weight losses may be due to decomposition of metal acrylate complex, which might have formed from acrylamide and metal nitrates. However, after 600 °C, there is no weight loss observed in TG curve, which

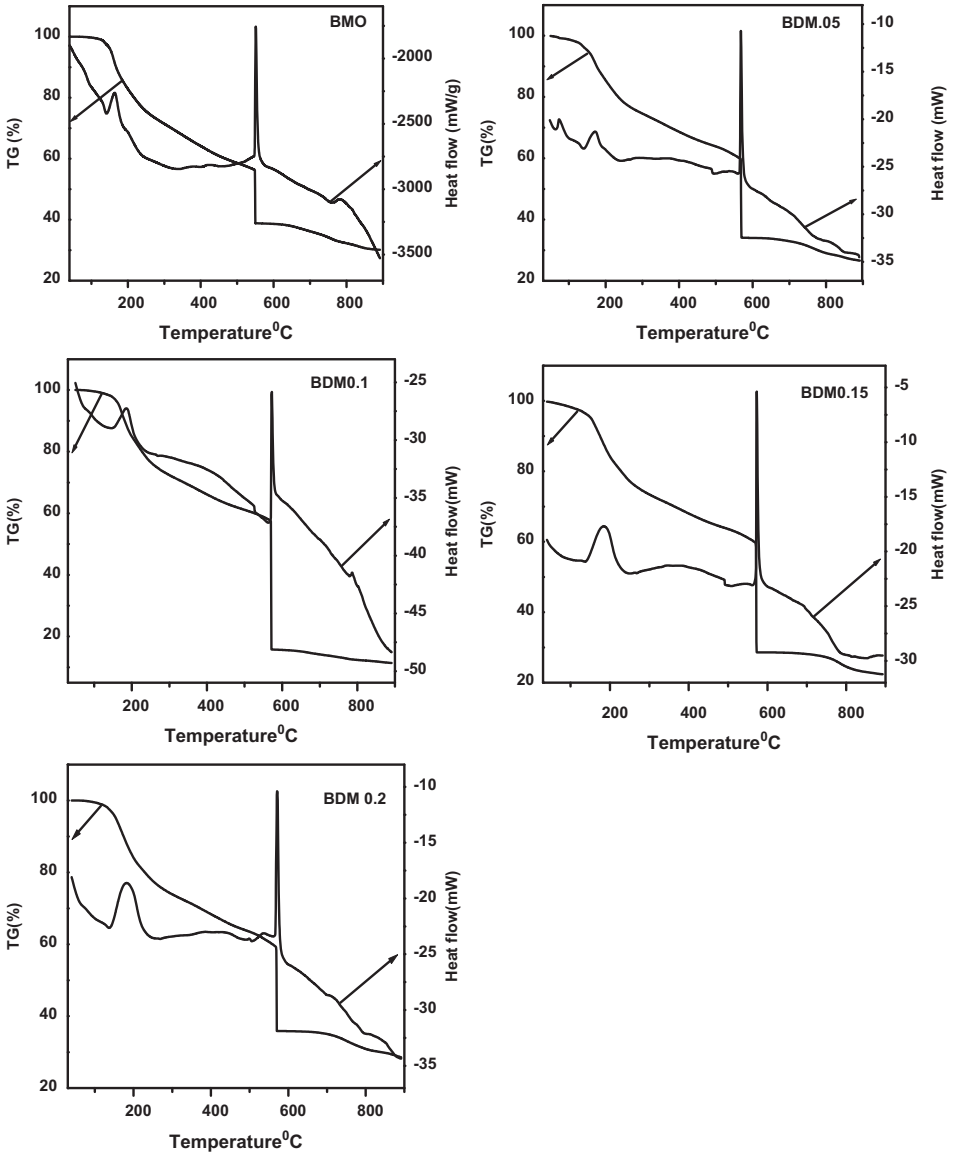

Fig. 1. TG/DTA curves for the dried gels of various compositions of Dy doped $BaMoO_4$ [$Ba_{1-x}Dy_xO_{4+\delta}$, where $x=0$ (BMO), 0.05 (BDM0.05), 0.1 (BDM0.1), 0.15 (BDM0.15), 0.2 (BDM0.2)] samples, heated from 30 to 900 °C.

indicates that there is complete decomposition of organic derivatives from the sample.

3.2. XRD

Fig. 2 shows the XRD patterns for $BaMoO_4$ sample calcined at different temperatures. At 250 °C, the observed XRD peaks are compared with the ICDD data (00-011-1144) and confirmed the formation of the barium nitrate crystalline phase. At 350 °C, the obtained XRD peaks are matched with the ICDD data (00-011-1144 for barium nitrate and 00-029-0193 for barium molybdate) and confirmed mixed phases of barium nitrate and also the barium molybdate. At higher calcined temperatures from 600 °C to 900 °C, Scheelite type pure crystalline $BaMoO_4$ phase is formed. The crystalline size of $BaMoO_4$ sample is calculated using Scherrer's

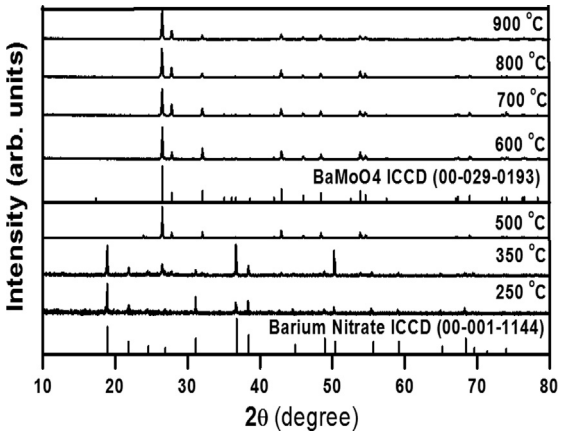

Fig. 2. XRD patterns for the $BaMoO_4$ gel sample, calcined at various temperatures.

formula; $D = 0.9\lambda/(\beta \cos\theta)$, where λ is the X-ray wave length (0.1548 nm), β is full width half maxima (FWHM) of the peak. The average crystallite size of $BaMoO_4$ is found to be ~60 nm. Fig. 3 shows the XRD patterns for the various compositions of Dy doped $BaMoO_4$ samples obtained at 900 °C. All the observed peaks are analyzed by comparing

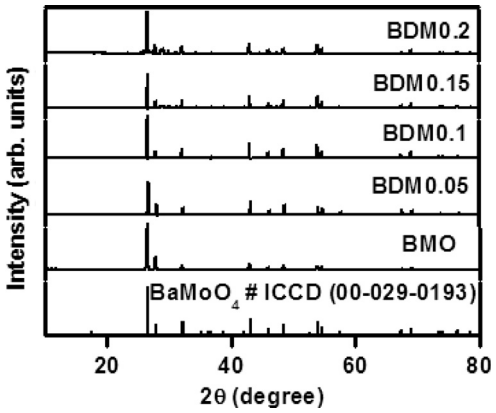

Fig. 3. XRD patterns for various compositions of Dy doped $BaMoO_4$ samples obtained at 900 °C.

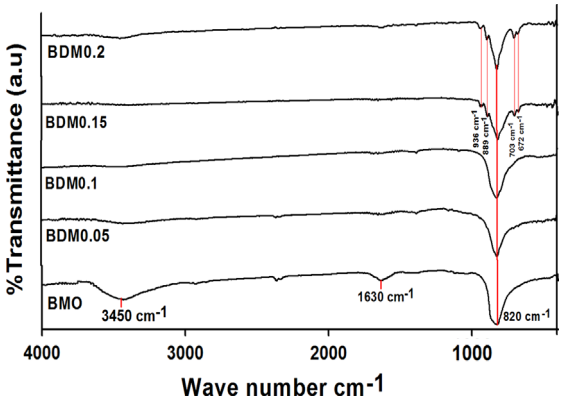

Fig. 4. FTIR spectra for various compositions of Dy doped $BaMoO_4$ samples, calcined at 900 °C.

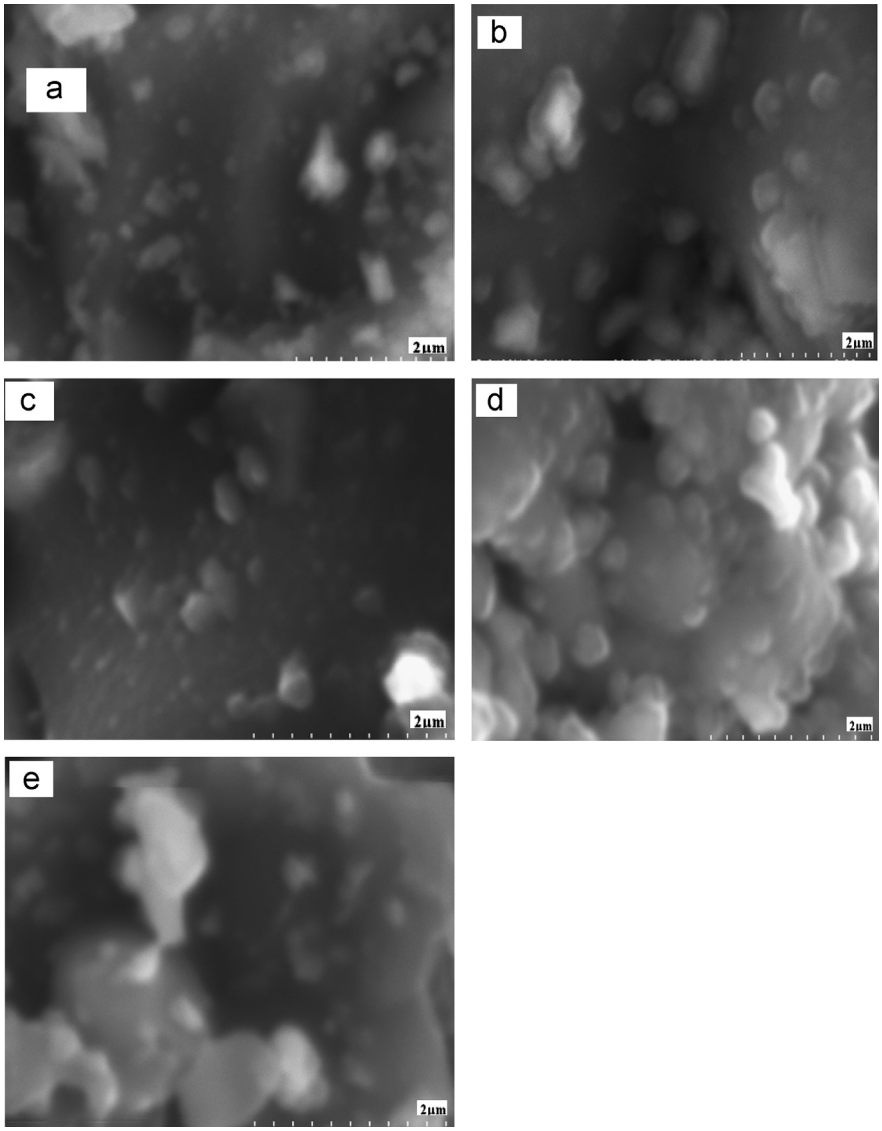

Fig. 5. SEM images for various compositions of Dy doped $BaMoO_4$ [where (a) BMO, (b) BDM0.05, (c) BDM0.1, (d) BDM0.15, and (e) BDM0.2] powder samples calcined at 900 °C.

with ICDD data (00-029-0193 for $BaMoO_4$). In Fig. 3, no additional peaks are observed within the composition $0 \leq x \geq 0.1$; indicating the doping of Dy^{3+} in Ba^{2+} site. For the samples, $x > 0.1$ indicating the slight additional diffraction peaks in the XRD patterns confirmed the formation of mixed crystalline phases at higher compositions. The average crystallite sizes of all compositions of Dy doped $BaMoO_4$ samples at 900 °C are found to be less than 100 nm.

3.3. FTIR

Fig. 4 shows FTIR spectra recorded for $BaMoO_4$ and various compositions Dy doped $BaMoO_4$ [$Ba_{1-x}Dy_xMoO_{4+x/2}$, where $x=0$ (BMO), 0.05 (BDM0.05), 0.1 (BDM0.1), 0.15 (BDM0.15), and 0.2 (BDM0.2)] samples calcined at 900 °C. For $BaMoO_4$ and all the compositions of Dy BaMoO4 samples, the appearance of the IR band at ~820 cm^{-1} is attributed to the Mo–O stretching vibration. When the

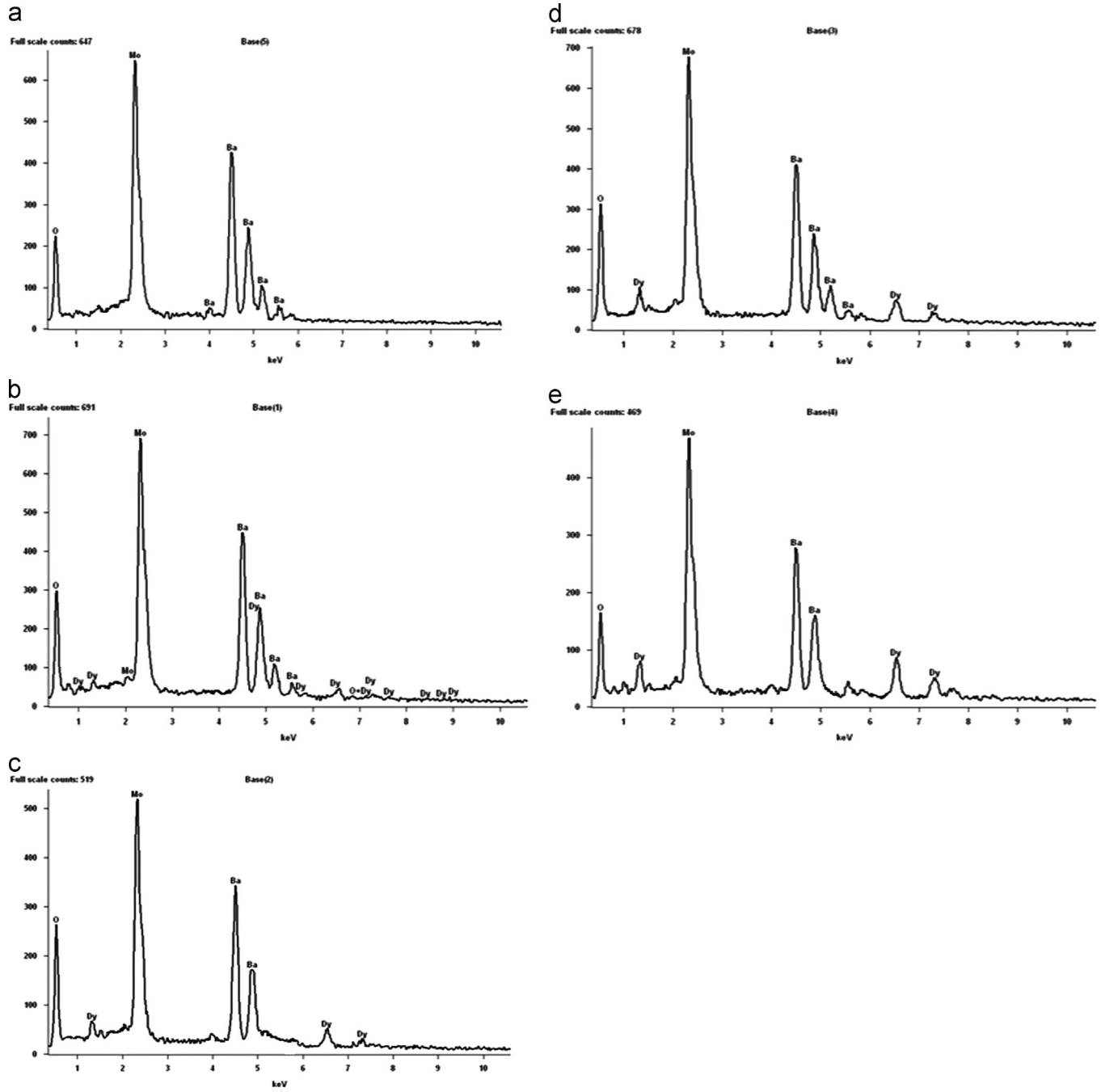

Fig. 6. EDX spectra for various compositions of Dy doped $BaMoO_4$ [where (a) BMO, (b) BDM0.05, (c) BDM0.1, (d) BDM0.15, and (e) BDM0.2] powder samples calcined at 900 °C.

dopant quantity increases, the defects concentration increases and hence, for the composition $x > 0.1$ samples, newly observed IR bands at 936 cm^{-1}, 889 cm^{-1}, 703 cm^{-1} and 672 cm^{-1} are due to the formation of Dy–O and Dy–O–Ba bonds. The IR bands observed at 3450 cm^{-1} and 1630 cm^{-1} of the BMO sample are due to stretching and bending vibration modes of O–H bonds in water molecules arising from the room atmosphere [25–27].

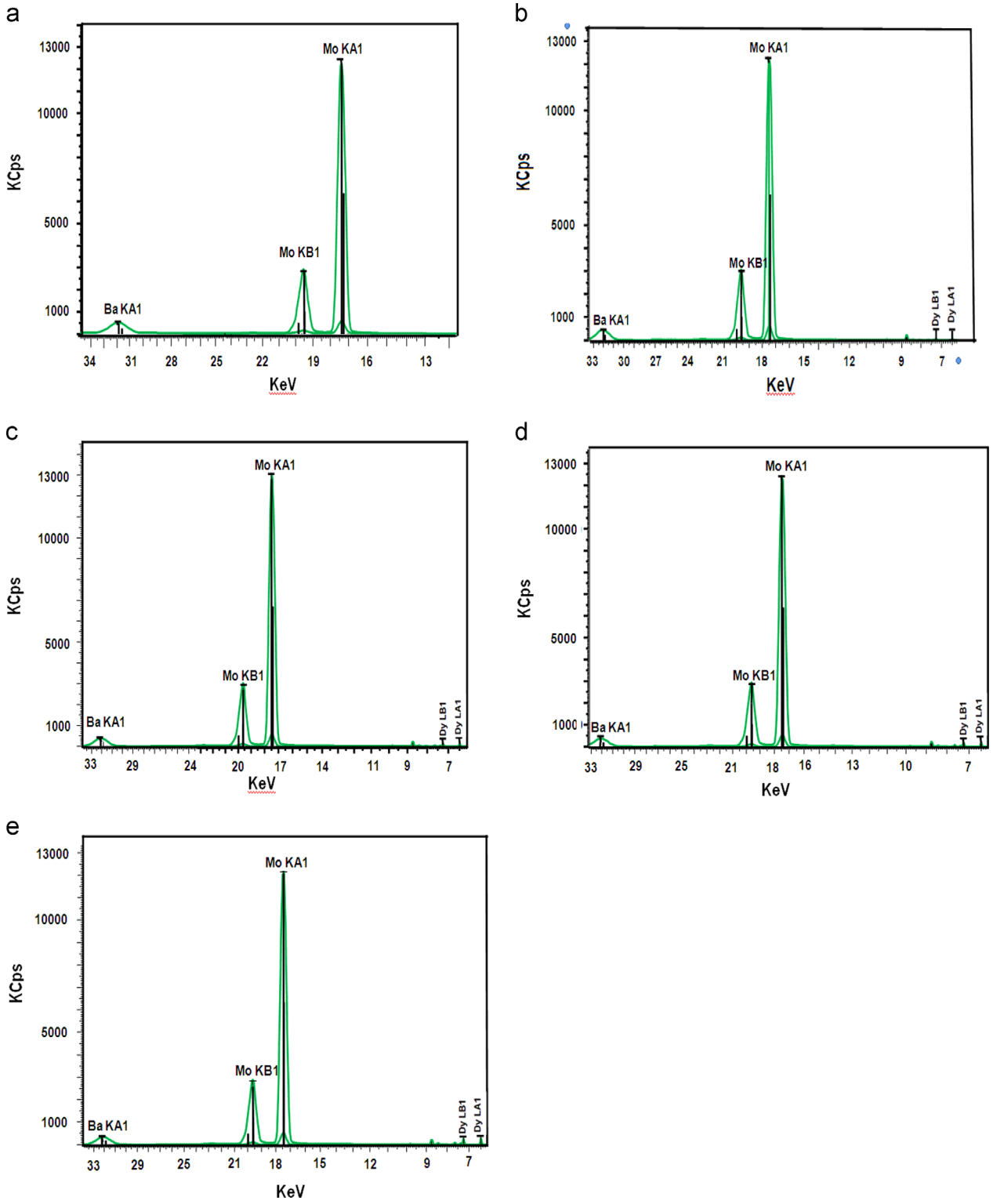

Fig. 7. XRF spectra for various compositions of Dy doped $BaMoO_4$ [where (a) BMO, (b) BDM0.05, (c) BDM0.1, (d) BDM0.15, and (e) BDM0.2] powder samples calcined at 900 °C.

Table 1
The percentages of the Dy_2O_3, BaO and MoO_3 exist in the $BaMoO_4$ and various compositions of Dy doped $BaMoO_4$ samples, obtained from XRF.

	BMO (%)	BDM0.05 (%)	BDM0.1 (%)	BDM0.15 (%)	BDM0.2 (%)
Dy_2O_3	–	3.06	5.77	8.37	12.18
BaO	55.93	50.08	45.24	44.10	39.48
MoO_3	42.70	45.45	47.60	46.86	46.89

3.4. SEM-EDX

Figs. 5 and 6 show the SEM images and EDX spectra for $BaMoO_4$ and various compositions of Dy doped $BaMoO_4$ [$Ba_{1-x}Dy_xMoO_{4+x/2}$, where x=0 (BMO), 0.05 (BDM0.05), 0.1 (BDM0.1), 0.15 (BDM0.15), and 0.2 (BDM0.2)] powder samples calcined at 900 °C respectively. SEM micrographs showed agglomerated particles of $BaMoO_4$ and various compositions of Dy doped $BaMoO_4$ powder samples and their measured particle sizes are found to be less than 200 nm. EDX spectra showed the existence of (O, Ba and Mo) in $BaMoO_4$ sample and (O, Dy, Mo and Ba) elements in Dy doped $BaMoO_4$ samples calcined at 900 °C.

3.5. X-ray fluorescence analysis

Fig. 7 shows the XRF spectra for $BaMoO_4$ and various compositions of Dy doped $BaMoO_4$ samples calcined at 900 °C. From the corresponding characteristic peaks, the presence of Dy, Ba, Mo and O elements identified are shown in Fig. 7. From the X-ray fluorescence spectra, the presence of Dy_2O_3, BaO and MoO_3 oxide elements are observed of the various composition of Dy doped $BaMoO_4$ samples. The percentages of existing Dy_2O_3, BaO and MoO_3 for all the composition are tabulated in Table 1. The percentage of the Dy_2O_3 increases and BaO decreases with increase of Dy doping in $BaMoO_4$ samples.

3.6. Impedance studies

Fig. 8(a–c) shows the complex impedance (imaginary $-Z''$ vs. real Z') plots at different temperatures ranging from 350 to 650 °C under air for the nanocrystalline $Ba_{.90}Dy_{0.10}MoO_{4+\delta}$ sample. The measured impedance data of the nanocrystalline Dy doped $BaMoO_4$ [$Ba_{1-x}Dy_xMoO_{4+\delta}$, where x=0, 0.05, 0.1, 0.15, and 0.2] samples are analyzed using winfit software and obtained the total resistance (R) of the sample. The resistance obtained from impedance plot is used to calculate the conductivity (σ) of the sample by using the relationship

$$\sigma = L/RA \quad (1)$$

where L is the thickness of the sample pellet and A is the area of the sample.

From Fig. 8(a–c) it is observed that with increase in temperature, the depressed semicircles shift towards the high frequency side of the abscissa, which indicate the resistance of the sample decreases hence the electrical conductivity of the sample increases. Fig. 9 shows the log (σT) vs. 1000/T plots of the nanocrystalline Dy doped $BaMoO_4$ [$Ba_{1-x}Dy_xMoO_{4+\delta}$, where x=0, 0.05, 0.1, 0.15, and 0.2] samples and the data

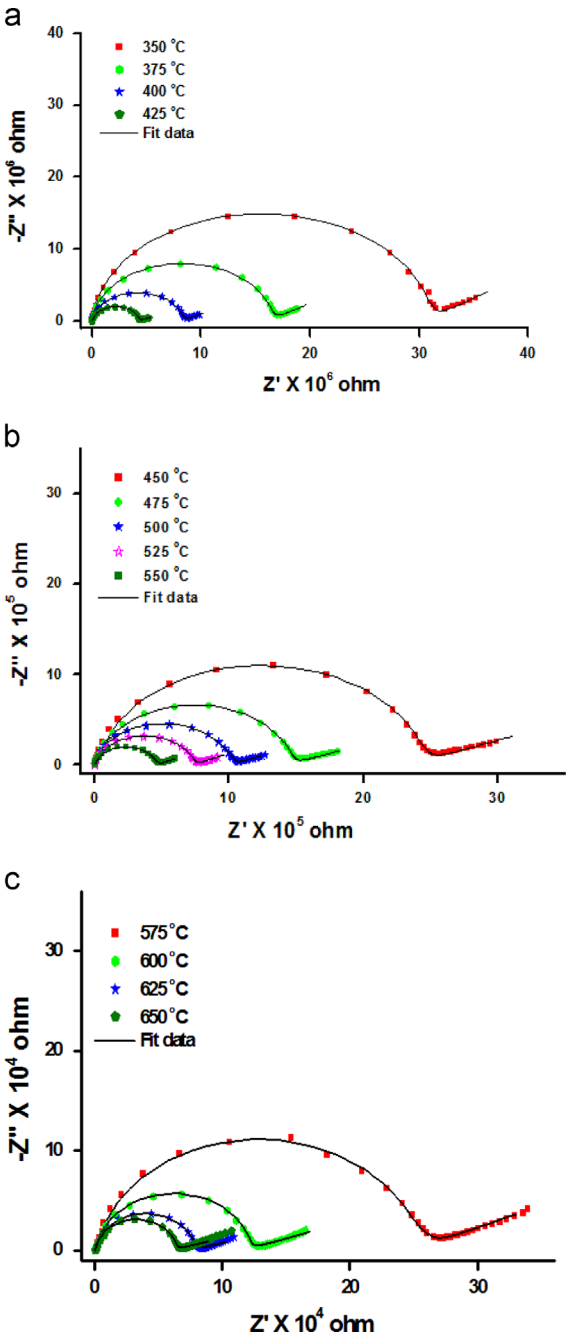

Fig. 8. (a–c) Impedance (Z' and $-Z''$) plots for the nanocrystalline $Ba_{0.90}Dy_{0.10}MoO_{4+\delta}$ sample measured at different temperatures.

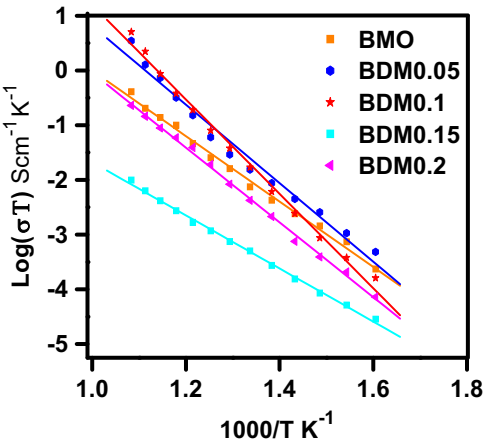

Fig. 9. Log σT vs. 1000/T for the various compositions of nanocrystalline Dy doped $BaMoO_4$ samples.

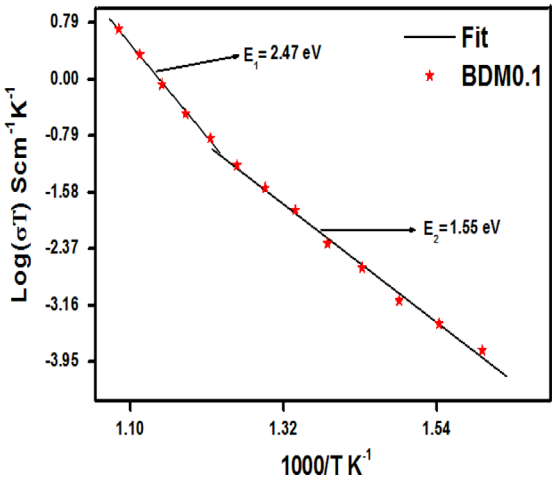

Fig. 11. Log (σT) vs. 1000/T shows the activation energies for $Ba_{0.90}Dy_{0.10}MoO_{4+\delta}$ sample in the two temperature regions.

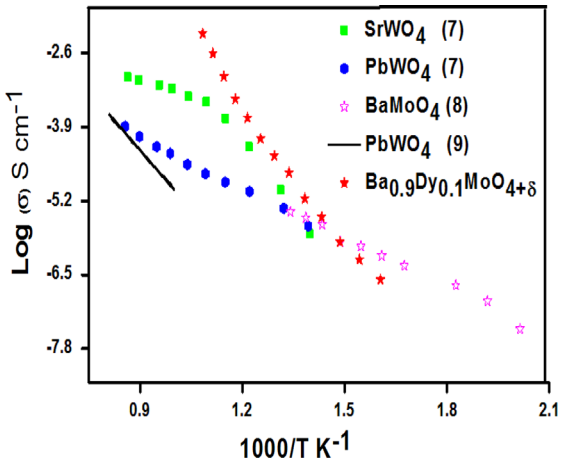

Fig. 10. Log σ vs. 1000/T plot for the nanocrystalline $Ba_{0.90}Dy_{0.10}MoO_{4+\delta}$ sample and other reported samples.

points are fitted to the Arrhenius equation

$$\sigma T = \sigma_0 \exp(-E_a/KT) \quad (2)$$

where, E_a and σ_0 are activation energy and temperature independent conductivity respectively. The activation energies for conduction of all compositions are calculated from the slopes of log (σT) vs. 1000/T plots in the temperature range 350–650 °C. The nanocrystalline $Ba_{0.90}Dy_{0.10}MoO_{4+\delta}$ composition sample showed the highest activation energy and conductivity compared to other compositions of the nanocrystalline Dy doped $BaMoO_4$ [$Ba_{1-x}Dy_xMoO_{4+\delta}$, where x=0, 0.05, 0.1, 0.15, and 0.2] samples. This is due to doping of Dysprosium (Dy^{3+}) in place Barium (Ba^{2+}) sites in $Ba_{1-x}Dy_xMoO_{4+\delta}$ (where x=0, 0.05, 0.1, 0.15, and 0.2) samples. The dysprosium concentration increases, which increase the total charge carrier concentration, hence enhance the ionic conductivity. The dysprosium doping does not alter its parent structure up to x=0.1 and slight changes in the phase at x=0.15 composition, which are confirmed from XRD results. Doping of dysprosium $>$ 0.15 forms the mixed phases of $BaMoO_4$, which are confirmed from XRD results. Hence, the conductivity increases linearly up to x=0.1 because of high charge carrier concentration. The observed higher activation energy may be due to the formation and migration of oxygen ion charge carriers, which may increase the conductivity of the nanocrystalline $Ba_{0.90}Dy_{0.10}MoO_{4+\delta}$ sample. Fig. 10 shows the log σ vs. 1000/T plots for the nanocrystalline $Ba_{0.90}Dy_{0.10}MoO_{4+\delta}$ and compared with the literature results. From Fig. 10, the newly prepared nanocrystalline $Ba_{0.90}Dy_{0.10}MoO_{4+\delta}$ showed the higher conductivity compared to the other reported pure Scheelite type nanocrystalline samples such as $SrWO_4$ [7], $BaMoO_4$ [8] and $PbWO_4$ [7,9].

Fig.11 shows the log (σT) vs. 1000/T plot for $Ba_{0.90}Dy_{0.10}MoO_{4+\delta}$ sample. In Fig. 11, the log (σT) vs. 1000/T plot showed the two regions and the activation energies are calculated for two regions of $Ba_{0.90}Dy_{0.10}MoO_{4+\delta}$ sample, which indicate the existence of two different conductivity mechanisms [11,15]. The conductivity at high temperature region ($>$ 525 °C) may be expressed as

$$\sigma T = \sigma_0 \exp(-E_1/T) \quad (3)$$

where E_1=(1/2)E_f+E_m, E_f and E_m are the activation energies of defect formation and migration of oxygen ion charge carriers.

The conductivity at low temperature region ($\leq$ 525 °C) may be expressed as

$$\sigma T = \sigma_0 \exp(-E_2/T) \quad (4)$$

where E_2=E_m is the activation energy required for the migration of oxygen ion charge carriers.

The defect formation energy E_f can be calculated from Eqs. (3) and (4).

$$E_f = 2(E_1 - E_2) \quad (5)$$

The activation energies in the two temperature regions for the nanocrystalline Dy doped $BaMoO_4$ [$Ba_{1-x}Dy_xMoO_{4+\delta}$, where x=0, 0.05, 0.1, 0.15, and 0.2] samples are calculated which

Table 2
Activation energies obtained from log σT vs. 1000/T of nanocrystalline $BaMoO_4$ and all the compositions of Dy doped $BaMoO_4$ samples.

	Activation energy (E_1) (ev) (Region I ≤ 525 °C)	Activation energy (E_2) (ev) (Region II > 525 °C)	Energy for the formation of defects (E_f) (ev)
BMO	1.10 ± 0.03	1.32 ± 0.11	0.44
BDM0.05	1.15 ± 0.02	1.99 ± 0.10	1.68
BDM0.1	1.55 ± 0.04	2.47 ± 0.02	1.84
BDM0.15	0.92 ± 0.01	1.15 ± 0.02	0.46
BDM0.2	1.16 ± 0.04	1.32 ± 0.04	0.32

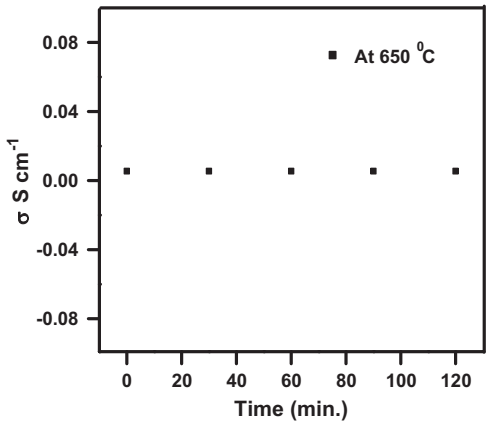

Fig. 12. Time vs. conductivity plot for the $Ba_{0.90}Dy_{0.10}MoO_{4+\delta}$ sample obtained at 650 °C.

are shown in Table 2. The nanocrystalline $Ba_{0.90}Dy_{0.10}MoO_{4+\delta}$ composition sample showed the highest defect formation energy compared to other compositions of the nanocrystalline Dy doped $BaMoO_4$ [$Ba_{1-x}Dy_xMoO_{4+\delta}$, where $x=0$, 0.05, 0.1, 0.15, and 0.2] samples, which may enhance the ionic conductivity of the particular composition and hence, showed the highest conductivity compared to the other compositions of the prepared samples.

The Fig. 12 shows the time vs. conductivity of the $Ba_{0.90}Dy_{0.10}MoO_{4+\delta}$ sample measured at 650 °C for every half an hour. It is observed that there is no change in conductivity plot with time which confirms that, the good stability of the sample at 650 °C under air.

4. Conclusions

Nanocrystalline Dy doped $BaMoO_4$ [$Ba_{1-x}Dy_xMoO_{4+\delta}$, where $x=0$, 0.05, 0.1, 0.15, and 0.2] samples were prepared by the acrylamide assisted sol–gel combustion process, which may be use as electrolyte for ITSOFCs application. Thermal behavior, structural information, phase formation and existence of O, Dy, Mo and Ba, elements in $Ba_{1-x}Dy_xMoO_4$ ($x=0$, 0.05, 0.1, 0.15, and 0.2) samples are investigated through TG/DTA, XRD, FTIR, SEM-EDX and XRF techniques respectively. The electrical conductivity of the prepared samples is studied through impedance spectroscopy. The doped Scheelite type nanocrystalline $Ba_{0.90}Dy_{0.10}MoO_{4+\delta}$ sample showed enhanced conductivity of 5.46×10^{-3} S/cm at 650 °C compared to the other reported Scheelite samples. The observed higher conductivity and higher activation energy may be due to the formation and migration of oxygen ion charge carriers in the Dy doped $BaMoO_4$ ($Ba_{0.90}Dy_{0.10}MoO_{4+\delta}$) sample.

Acknowledgments

Dr. N.S. gratefully acknowledges DST, AICTE, UGC, CSIR and DRDO, Government of India, for receiving financial support in the form of major research projects. Authors would like to thank Central Instrumentation Facility (CIF), Pondicherry University for using TG/DTA, SEM-EDX and XRF facilities for the present work.

References

[1] J.P.P. Huijsmans, Ceramics in solid oxide fuel cells, Current Opinion in Solid State and Materials Science 5 (2001) 317–323.
[2] P.N. Dyer, R.E. Rechards, S.L. Russek, D.M. Taylor, Ion transport membrane technology for oxygen separation and syngas production, Solid State Ionics 134 (2000) 21–33.
[3] Jonn B. Goodenough, Oxide-ion electrolytes, Annual Review of Materials Research 33 (2003) 91–128.
[4] V.V. Kharton, F.M.B. Marquesa, A. Atkinson, Transport properties of oxide electrolyte ceramics: a brief review, Solid State Ionics 174 (2004) 135–149.
[5] G.G Zang, Q.F Fang, X.P Wang, Z.G Yi, Dielectric relaxation study of $Pb_{1-x}La_xMoO_{4+\delta}$ ($x=0$–0.3) oxide-ion conductors, Journal of Physics: Condensed Matter 15 (2003) 4135–4242.
[6] Roscoe G. Dickinson, The crystal structure of wulfenite and scheelite, Journal of the American Chemical Society 42 (1) (1920) 85–93.
[7] V. Thangadurai, C. Knittlmayer, W. Weppner, Metathetic room temperature preparation and characterization of scheelite-type ABO_4 (A=Ca, Sr, Ba; B=Mo, W) powers, Materials Science and Engineering B 106 (2004) 228–233.
[8] N. Nallamuthu, I. Prakash, N. Satyanarayana, M. Venketeswarlu, Preparation, characterization and electrical conductivity studies of nanocrystalline La doped $BaMoO_4$, Materials Research Bulletin 46 (2011) 32–41.
[9] T. Esaka, Ionic conduction in substituted scheelite-type oxides, Solid State Ionics 136–137 (2000) 1–9.
[10] Jihai Cheng, Weito Bao, Chengliang Han, Wenbing Cao, A novel electrolyte for intermediate solid oxide fuel cells, Journal of Power Sources 195 (2010) 1849–1853.
[11] Jihai Cheng, Chenfei Liua, Wenbing Cao, Mingixing Qi, Guoquan Shao, Synthesis and electrical properties of scheelite $Ca_{1-x}Sm_xMoO_{4+\delta}$ solid electrolytes ceramics, Materials Research Bulletin 46 (2011) 185–189.
[12] Takao Esaka, Ryoichi Tachibana, Sigeomi Takai, Oxide ion conduction in the Sm-substituted $PbWoO_4$ phases, Solid State Ionics 92 (1996) 129–133.
[13] S. Takaim, T. Adachi, T. Esaka, Investigation of the localized oxide ion interstitials of $PbWO_4$-based oxide ion conductors by means of impedance spectroscopy, Materials Research Bulleitin 41 (2006) 2088–2093.

[14] Shigeomi Takai, Kenji Sugiura, Takao Esaka, Ionic conduction properties of $Pb_{1-x}M_xWO_{4+\delta}$ (M=Pr and Tb), Materials Research Bulletin 34 (1999) 193–202.
[15] S.K. Arora, R.S. Godbole, D. Lakshminarayana, Lattice disorder and electrical conductivity of flux-grown $Ca(WO_4)_x(MoO_4)_{1-x}$ crystals, Journal of Materials Science 18 (1983) 1359–1364.
[16] Martin G. Bellino, Diegeo G. Lamas, Noemi E. Walsoe de Reca, Enhanced Ionic Conductivity in Nanostructured, Heavily Doped Ceria Ceramics, Advanced Funtional Materials 16 (2006) 107–113.
[17] H.N. Chang, J.G. Duh, S.R Sheeen, $LiMn_2O_4$ cathode doped with excess lithium and synthesized by co-precipitation for Li-ion batteries, Journal of Power Sources 115 (2003) 110–118.
[18] N. Nallamuthu, I. Prakash, M. Venkateswarlu, S. Balsubramaniyam, N. Satyanarayana, Sol–gel synthesis and characterization of Li_2O–As_2O_5–SiO_2 glassy system, Materials Chemistry and Physics 111 (2008) 24–28.
[19] Guangzhi Li, Zhenling Wang, Zewei Quan, Chunxia Li, Jun Lin, Growth of highly crystalline $CaMoO_4$:Tb^{3+} phosphor layers on spherical SiO_2 particles via sol–gel process: structural characterization and luminescent properties, Crystal Growth and Design 7 (9) (2007) 1082–1797.
[20] Hsin-Lung Lin, Ray-Kuang Chiang, Wei-Te Li, Low-temperature synthesis of pure $BaAl_2Si_2O_8$ glass-ceramic power by citrate process, Journal of Non-Crystalline Solids 351 (2005) 3044–3049.
[21] X. Guo, P. Sujatha Devi, B.G. Ravi, J.B. Parise, S. Sampath, J.C. Hanson, Phase evolution of yttrium aluminium garnet (YAG) in a citrate–nitrate gel combustion process, Journal of Materials Chemistry 14 (2004) 1288–1292.
[22] W.D Yang, Y.H. Chang, S.H Huang, Influence of molar ratio of citric acid to metal ions on preparation of $La_{0.67}Sr_{0.33}MnO_3$ materials via polymerizable complex, Journal of the European Ceramic Society 25 (2005) 3611–3618.
[23] K. Du, H. Zhang, Preparation and performance of spinel $LiMn_2O_4$ by a citrate rout with combustion, Journal of Alloys and Compounds 352 (2003) 250–254.
[24] S. Vivekananda, M. Venketeswarlu, N. Satyanarayana, Novel urea assisted polymeric citrate route for the synthesis of nanocrystalline spinel $LiMn_2O_4$ powers, Journal of Alloys and Compounds 441 (2007) 284–290.
[25] S. George, Infrared and Raman Characteristics Group Frequencies Tables and Charts, third ed., John Wiley and Sons, England, 2001.
[26] J.C. Sczancoski, L.S. Cavalcante, N.L. Maran, R.O. da Silva, R.L. Tranquilin, M.R. Joya, P.S. Pizani, J.A. Varala, J.R. Sambrano, M. Siu Li, E. Longo, J. Andres, Electronic structure and optical properties of $BaMoO_4$ powers, Current Applied Physics 10 (2010) 614–624.
[27] R.K. Khanna, E.R. Lippincott, Infrared spectra of some scheelite structures, Spectrochimica Acta 24A (1968) 905–908.